



# Fe<sub>2</sub>O<sub>3</sub>/hemp straw-based porous carbon composite for supercapacitor electrode materials

Xia Jiang<sup>1,2</sup> · Gaofeng Shi<sup>1</sup> · Guoying Wang<sup>1</sup> · Puranjan Mishra<sup>3</sup> · Jianwen Du<sup>2</sup> · Yu Zhang<sup>2</sup>

Received: 26 February 2020 / Accepted: 27 March 2020 / Published online: 20 May 2020  
© Springer-Verlag GmbH Germany, part of Springer Nature 2020

## Abstract

The porous activated carbon material was prepared using hemp straw as the biomass carbon source, which was used as the substrate material to synthesize Fe<sub>2</sub>O<sub>3</sub>/porous carbon nanocomposites (Fe<sub>2</sub>O<sub>3</sub>/HAC) by simple and effective hydrothermal method. The results show that the porous activated carbon based on hemp straw is an ideal substrate for Fe<sub>2</sub>O<sub>3</sub>, which can effectively avoid the agglomeration of metal oxides, increase the contact area with electrolyte, and shorten the ion diffusion path, so as to improve the electrochemical performance of the material. In three-electrode system, the electrochemical performance of Fe<sub>2</sub>O<sub>3</sub>/HAC is much higher than that of HAC and Fe<sub>2</sub>O<sub>3</sub> alone. At the current density of 1 A g<sup>-1</sup>, its specific capacitance is 256 F g<sup>-1</sup>, and it has the best capacity retention. The symmetrical device composed of the material has a good capacitance value and excellent cycle stability.

**Keywords** Iron oxide · Activated carbon · Composite material · Supercapacitor

## 1. Introduction

Supercapacitor is a new type of energy storage device, due to its high-power density, fast charge-discharge rate, and long cycle life, which is widely used in various fields [1, 2]. Electrode material is an important part of supercapacitor. Therefore, the high-efficiency electrode material is very necessary for the construction of supercapacitor. According to different storage mechanisms, supercapacitors can be divided into two types: double-layer capacitors and pseudocapacitors. In double-layer capacitors, the electrode materials are mainly carbon materials such as activated carbon [3], graphene [4], and carbon nanotubes [5, 6]. Biomass carbon materials are widely used as electrode materials for double-layer capacitors

due to their wide sources, low cost, and low environmental pollution. Carbon materials have stable electrochemical properties and good electrical conductivity but have low capacity and low-energy density [7–10]. Metal oxides [11–13] and conducting polymers [14–16] are used as pseudocapacitor materials. Metal oxides in electrode materials have a large specific capacitance and energy density [17–20]. Among all kinds of metal oxide electrode materials, iron-based compounds have broad application prospects in energy storage equipment due to their large theoretical capacity (3625 F g<sup>-1</sup>), natural abundance, easy to obtain, and environment friendly [21–23]. However, the crystal structure defects of iron-based materials affect the electrical conductivity and structural stability in practical applications, which severely limit its capacitance performance and cycle life. Therefore, carbon-based materials are used as carbon framework to load metal oxides uniformly. In this way, the carbon framework provides stable loading site for metal oxides, while its porous structure channels are conducive to the ion transport in the electrolyte and provide part of the double electric layer capacitance. Metal oxides are also well dispersed and play a greater role in pseudocapacitance. Finally, through the synergistic effect of the double-layer capacitor and the pseudocapacitor, the quality, capacity, and cycle stability of the electrode can be effectively improved. It has been reported that this kind of hybrid material supercapacitor has achieved good results.

✉ Gaofeng Shi  
gaofengshi\_lzh@163.com

✉ Guoying Wang  
wangguoying@lut.edu.cn

<sup>1</sup> School of Petrochemical Engineering, Lanzhou University of Technology, Lanzhou, China

<sup>2</sup> Gansu Vocational College of Agriculture, Lanzhou, China

<sup>3</sup> Faculty of Engineering Technology, University Malaysia Pahang, Lebuhraya Tun Razak, 26300 Gambang, Kuantan, Pahang, Malaysia

For example, K. K. Lee [24] fabricated a nanocomposite comprising  $\alpha$ -Fe<sub>2</sub>O<sub>3</sub> nanotubes (NTs) anchored on reduced graphene oxide for electrochemical capacitors. The hollow tubular structure of the  $\alpha$ -Fe<sub>2</sub>O<sub>3</sub> NTs presents a high surface area for reaction; the nanocomposite materials exhibit a specific capacitance which is remarkably higher than  $\alpha$ -Fe<sub>2</sub>O<sub>3</sub> alone. Low Q X [25] prepared the composite material of Fe<sub>2</sub>O<sub>3</sub> and graphene oxide by a hydrothermal method, using as electrode material. The nanocomposite exhibits pseudo capacitive properties of high specific capacitance similar to 504 F g<sup>-1</sup> at 2 mA cm<sup>2</sup>. Balasubramanian Sethuraman [26] utilized a simple and template-free green route for the production of biocompatible reticulated Fe<sub>2</sub>O<sub>3</sub>/C nanocomposites based on natural polysaccharides for supercapacitors. At the current density of 2 mV s<sup>-1</sup>, its specific capacitance is 256 F g<sup>-1</sup>, indicating that the Fe<sub>2</sub>O<sub>3</sub>/C composite can be used as a promising electroactive material for supercapacitors.

Hemp is a vigorous crop, which has a large planting area in the western part of Gansu Province [27]. However, the hemp straw has not been effectively developed and utilized; most of them has been discarded or burned, which not only causes the waste of biomass resources but also pollutes the environment, so the hemp straw has not been used with high value. Therefore, in this work, we used hemp straw as a source of biomass carbon and composited with Fe<sub>2</sub>O<sub>3</sub> to produce high-value, high-performance supercapacitor electrode materials, which are of great significance. Firstly, hemp straw was used as carbon source and KOH was used as pore-expanding agent, the porous activated carbon material was prepared, and this material was used as the carbon framework for iron-based compound. The Fe<sub>2</sub>O<sub>3</sub> nanostructure composite was synthesized by hydrothermal method. Because of the porous activated carbon based on hemp straw, it has interconnected pore structures with different sizes, and the formed ferrite is evenly and stably embedded in the cavity of the activated carbon to effectively avoid the agglomeration of metal oxides. At the same time, the material is more favorable for increasing the contact area with the electrolyte and shortening the ion diffusion path. Therefore, hemp straw-based porous activated carbon is an ideal substrate for active substances, which greatly improves the internal resistance and poor cycle performance of Fe<sub>2</sub>O<sub>3</sub> and exhibits excellent capacitance performance.

## 2. Experimental section

### 2.1. Chemicals and reagents

All chemicals used in this work were of analytical reagent (AR) grade. Hemp straw was obtained from Tianshui City, Gansu Province, China. The potassium hydroxide (KOH), ferrous sulfate (FeSO<sub>4</sub>·7H<sub>2</sub>O), hydrogen peroxide (H<sub>2</sub>O<sub>2</sub>), ammonia (NH<sub>3</sub>·H<sub>2</sub>O), polyethylene glycol, carbon black,

and polytetrafluoroethylene (PTFE) were purchased from Chemical Reagent Co., Ltd. Deionized water (purified by Millipore-Q system) was used throughout the experiment.

### 2.2. Experimental details

- (1) Hemp straw was dried in the oven at 80 °C after pretreatment of washing. The dried hemp straw was crushed for 100 mesh. Through the optimization of the conditions, hemp straw powder and KOH were mixed uniformly according to a mass ratio of 1:2 and fully ground. Then, the mixed powder is transferred to the tubular furnace, carbonized at 800 °C for 2 h under the N<sub>2</sub> with the heating rate of 2 °C min<sup>-1</sup>. After that, the carbonized samples were washed with 15 wt% HCl solution and deionized water, dried at 60 °C for 12 h to obtain hemp straw-based activated carbon, which was named as HAC.
- (2) A 0.5 g of HAC was dispersed in 30 ml deionized water and sonicated for 30 min to make the HAC evenly dispersed. A 1.0 g of FeSO<sub>4</sub>·7H<sub>2</sub>O and 6 ml of polyethylene glycol were added to the above solution, and the ultrasonic treatment was continued for 30 min, and then 2.5 wt% NH<sub>3</sub>·H<sub>2</sub>O solution and 0.2 ml H<sub>2</sub>O<sub>2</sub> were added with sufficient stirring. With full stirring, it was transferred to a 100 ml autoclave and reacted at 160 °C for 9 h. After the reaction, the mixture was centrifuged, washed with deionized water, and dried at 60 °C for 12 h to obtain the iron-based porous activated carbon product, which was named as Fe<sub>2</sub>O<sub>3</sub>/HAC.
- (3) For performance comparison, Fe<sub>2</sub>O<sub>3</sub> nanoparticles were prepared using the same method and conditions, named as Fe<sub>2</sub>O<sub>3</sub>, which means that the preparation process was the same as Fe<sub>2</sub>O<sub>3</sub>/HAC, but HAC was not added.

### 2.3. Structure characterization

The morphology and microstructure were characterized by scanning electron microscope (SEM, JSM-6701F, Japan Electronics Co., Ltd.), transmission electron microscope (TEM, TECNAI G2 TF20, American FEI Corporation) units, X-ray photoelectron spectroscopy (XPS, PHI5702, USA), X-ray electron diffraction (XRD, D/Max-2400 Rigaku Corporation), Raman spectroscopy (Raman, Renishaw in via, Renishaw, UK), and Fourier infrared spectroscopy (FTIR, Nexus 670, Thermo Nicolet, USA) and were used for structural analysis. The specific surface area was measured by using N<sub>2</sub> adsorption-desorption test (BET, type ASAP2020, American Micromeritics Company) at 77.3 K.

## 2.4. Test of electrochemical properties

In three-electrode system, electrochemical measurements were carried out on a CHI660E electrochemical workstation (Shanghai Chenhua Instrument Co., Ltd.). The three-electrode system included platinum foil as the counter electrode, Hg/HgO electrode as the reference electrode, and 6 mol l<sup>-1</sup> KOH solution as the electrolyte.

The working electrodes were fabricated by mixing as-prepared carbon material (0.0040 g), acetylene black and polyvinylidene fluoride (PTFE) with a mass ratio of 85:10:5 in ethanol. The slurry was loaded onto nickel foam, dried at 60 °C for 12 h, and then pressurized at 8 MPa to obtain the working electrode.

For the three electrode configuration, specific capacitance of the electrode materials was calculated by Eq. (1):

$$C = \frac{I\Delta t}{m\Delta V} \quad (1)$$

where  $I$  refers discharge current (A),  $\Delta t$  refers discharge time (s),  $m$  refers the mass of electrode (g), and  $\Delta V$  refers voltage window (V) [28].

In two electrode system, a symmetrical supercapacitor device is assembled using the prepared material as an electrode material. The membrane (PP/PE composite membrane), 6 mol l<sup>-1</sup> KOH electrolyte, and the prepared materials material on the nickel sheet are symmetrically assembled into an electrode/membrane/electrode structure. Cyclic voltammetry (CV), constant current charge-discharge (GCD), and impedance (EIS) were tested on a chi660E electrochemical workstation. Cyclic stability was tested with a computer-controlled supercapacitor test system (Neware 5v0.1a, Shenzhen, China).

Calculating the mass ratio of the supercapacitor for the two-electrode condition by Eq. (2):

$$C = \frac{I\Delta t}{2m\Delta u} \quad (2)$$

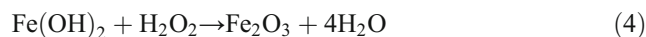
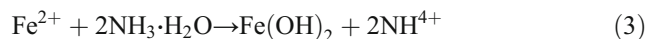
where  $\Delta t$  refers the discharge time,  $I$  refers the discharge current,  $m$  refers the mass of the working electrode, and  $\Delta u$  refers the voltage variation range [29].

## 3. Results and discussion

### 3.1. Formation of Fe<sub>2</sub>O<sub>3</sub>/HAC

As shown in Fig. 1, the pretreated hemp straw powder and KOH were mixed uniformly at a ratio of 1:2 and then carbonized at 800 °C under the N<sub>2</sub> to form porous activated carbon HAC with rich pore structure, which is used as the carrier of ferrite. As can be seen from the infrared spectrum of the HAC

in Fig. 2, there are obvious peaks at 1228 cm<sup>-1</sup>, 1594 cm<sup>-1</sup>, and 3450 cm<sup>-1</sup>, which correspond to -CO, -C=C, and -OH, respectively [30]. The results show that there are abundant of oxygen-containing groups and unsaturated groups on the surface of the HAC material, and these functional groups as the active sites in the carrier combine with Fe<sup>2+</sup> of FeSO<sub>4</sub> in the reaction solution. According to the literature, under the weak alkaline condition provided by NH<sub>3</sub>·H<sub>2</sub>O, Fe<sup>2+</sup> is oxidized to Fe<sup>3+</sup> by H<sub>2</sub>O<sub>2</sub>. The reaction formula is as follows [31]:

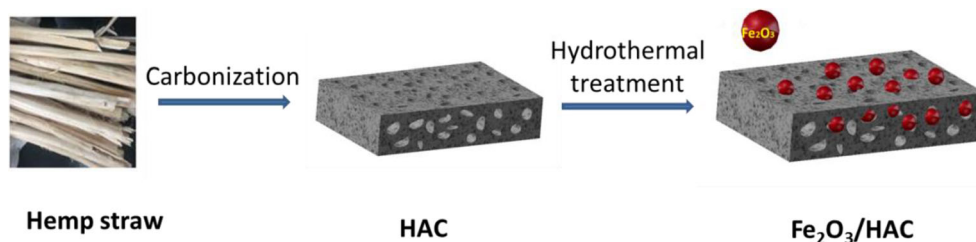


Through the above reaction process, Fe<sub>2</sub>O<sub>3</sub> is uniformly loaded on the HAC material, and part of the Fe<sub>2</sub>O<sub>3</sub> nanoparticles occupy the pores of the porous activated carbon HAC, so that Fe<sub>2</sub>O<sub>3</sub> is more firmly embedded in the HAC carrier. Therefore, while Fe<sub>2</sub>O<sub>3</sub> metal ions exert the performance of pseudocapacitance, the high conductivity and high porosity of the HAC are the key factors to improving electrochemical performance.

### 3.2. Material morphology and structure characterization

Firstly, the morphology of the HAC and the Fe<sub>2</sub>O<sub>3</sub>/HAC was performed by SEM and TEM, as shown in Fig. 3. According to literature reports, KOH has etching effect on carbon materials, forming a rich pore structure on the surface and inside of the materials [32]. Figure 3a shows the SEM image of the HAC. We can see that after the action of KOH etching, a large number of micropores and mesopores are formed on the carbon material, and these holes are evenly distributed throughout the HAC. These pore structures greatly increase the specific surface area of the activated carbon material, thereby increasing the contact area between the material and the electrolyte solution. As can be seen in Fig. 3b, Fe<sub>2</sub>O<sub>3</sub> nanoparticles synthesized by hydrothermal method are firmly attached to the HAC substrate, with uniform particle size and good dispersion. In Fig. 3c, the TEM image shows that the surface of the HAC is uneven and there are obvious holes, which can prove the existence of a large number of micropores and mesopores. In Fig. 3d, it can be seen that Fe<sub>2</sub>O<sub>3</sub> nanoparticles are uniformly dispersed in a carbon matrix with rich pore structure. Although we still see some larger particle clusters, which are composed of smaller nanoparticles, the surface of these Fe<sub>2</sub>O<sub>3</sub> nanoparticle clusters are porous and penetrable by the electrolyte. Overall, Fe<sub>2</sub>O<sub>3</sub> has good dispersibility. Therefore, through the SEM and TEM images of the HAC and Fe<sub>2</sub>O<sub>3</sub>/HAC, the abundant pore structure of the HAC and the homogeneous dispersion of Fe<sub>2</sub>O<sub>3</sub> nanoparticles in the Fe<sub>2</sub>O<sub>3</sub>/HAC are proved.

**Fig. 1** The formation mechanism of the Fe<sub>2</sub>O<sub>3</sub>/HAC



The HRTEM image of the Fe<sub>2</sub>O<sub>3</sub>/HAC is shown in Fig. 4a, it can be clearly seen that the pore structure shows bright interphases, and there are ordered stripes along the crystal plane direction, which has a higher degree of order, and shows a lattice spacing of 0.36 nm, corresponds to the (012) plane of  $\alpha$ -Fe<sub>2</sub>O<sub>3</sub> [33]. The high crystallization characteristics of  $\alpha$ -Fe<sub>2</sub>O<sub>3</sub> nanoparticles are confirmed by the selected regional electron diffraction (SAED) mode as shown in Fig. 4b. It shows a set of concentric rings, which can be indexed as (104), (113), (116), and (300) diffraction of diamond  $\alpha$ -Fe<sub>2</sub>O<sub>3</sub> [34].

Figure 5(a–d) shows the EDX mapping of C, O, and Fe elements in the Fe<sub>2</sub>O<sub>3</sub>/HAC, respectively. Obviously, C, O, and Fe elements are uniformly distributed in the Fe<sub>2</sub>O<sub>3</sub>/HAC composite, which further confirms the uniformity of Fe<sub>2</sub>O<sub>3</sub> nanoparticle dispersion. From the above SEM, TEM, and HRTEM image analysis, it can be seen that the Fe<sub>2</sub>O<sub>3</sub> nanoparticles formed by hydrothermal synthesis are uniformly embedded in the HAC prepared from hemp straw. Therefore, due to the rich pore structure of HAC in the Fe<sub>2</sub>O<sub>3</sub>/HAC materials, it can provide fast channel for ion transport and effectively improve the electrochemical performance of the materials.

The nitrogen adsorption-desorption isotherms and the pore size distribution for the HAC and Fe<sub>2</sub>O<sub>3</sub>/HAC were measured at 77 K, as shown in Fig. 6. According to the classification of the International Federation of Pure and Applied Chemistry

(IUPAC) [35], the adsorption-desorption curves of the HAC and Fe<sub>2</sub>O<sub>3</sub>/HAC belong to the mixed curves of I and IV, indicating that the HAC and Fe<sub>2</sub>O<sub>3</sub>/HAC have uniform microporous and mesoporous structures. As shown in Fig. 6a, in the low pressure region ( $P/P_0 = 0-0.02$ ), the curve of the HAC adsorption of N<sub>2</sub> is relatively steep, which indicates that there are a lot of micropores in the structure of HAC. In the medium pressure region ( $P/P_0 = 0.4-0.7$ ), the isothermal curves of the HAC and Fe<sub>2</sub>O<sub>3</sub>/HAC have obvious desorption hysteresis, and the Fe<sub>2</sub>O<sub>3</sub>/HAC is more significant, which indicates that there are mesopores in the structure of the HAC and Fe<sub>2</sub>O<sub>3</sub>/HAC [36]. Therefore, we can confirm that there are microporous and mesoporous structures in the HAC and Fe<sub>2</sub>O<sub>3</sub>/HAC. The pore size distribution curves of the HAC and Fe<sub>2</sub>O<sub>3</sub>/HAC calculated by the Barrett-Joyner-Halenda (BJH) method are shown in Fig. 6b. We can see that both the HAC and Fe<sub>2</sub>O<sub>3</sub>/HAC have continuous pore size distributions. The calculated pore size distribution data of the HAC and Fe<sub>2</sub>O<sub>3</sub>/HAC are shown in Table 1. We can see that compared with Fe<sub>2</sub>O<sub>3</sub>/HAC, HAC has a larger BET-specific surface area and pore volume, so we can further prove that the Fe<sub>2</sub>O<sub>3</sub> nanoparticles formed by hydrothermal are firmly embedded in the pores of the HAC, and they still have pores of 366.82 m<sup>2</sup> g<sup>-1</sup>, which provide favorable channels for electrolyte storage and ion transmission, further improving the electrochemical performance of the composite.

In the XRD analysis of Fig. 7a, the diffraction peaks of the HAC at 25° and 43° at 2 $\theta$  correspond to (002) and (100) lattice planes of graphite carbon, respectively, indicating the presence of disordered carbon structure [37]. Except for the obvious carbon peaks of the Fe<sub>2</sub>O<sub>3</sub>/HAC, most of the diffraction peaks correspond to the diffraction peaks of  $\alpha$ -Fe<sub>2</sub>O<sub>3</sub> (JCPDS No. 33-0664). The lattice parameters of  $\alpha$ -Fe<sub>2</sub>O<sub>3</sub> are  $a = 5.037$ ,  $B = 2.490$ ,  $C = 13.7$  [38, 39]. This result is very close to previous literature values [40]. Moreover, a small amount of Fe<sub>3</sub>C phase (JCPDS No. 75-910) emerged, which is easily formed at interfaces between iron/carbon and iron oxide/carbon during the hydrothermal process [41]. This result analysis can prove that the sample is a complex of HAC and Fe<sub>2</sub>O<sub>3</sub>. At the same time, we can see that the diffraction peaks of Fe<sub>2</sub>O<sub>3</sub> are consistent with  $\alpha$ -Fe<sub>2</sub>O<sub>3</sub>, which better illustrates the hydrothermal synthesis of  $\alpha$ -Fe<sub>2</sub>O<sub>3</sub> nanoparticles.

In order to further confirm the formation of the Fe<sub>2</sub>O<sub>3</sub>/HAC composites, we performed Raman characterization, as shown

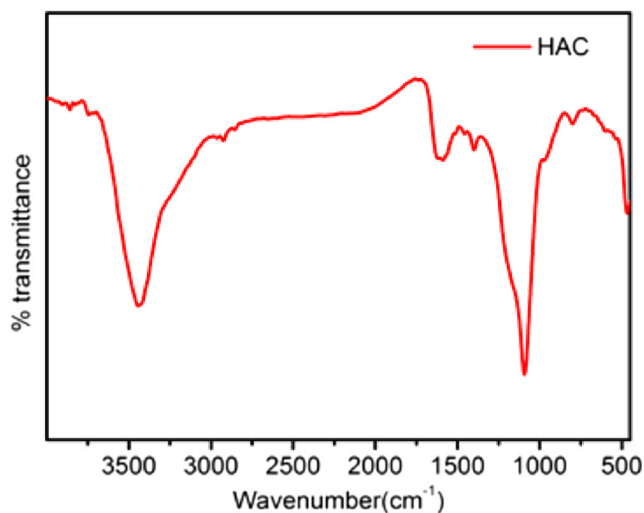
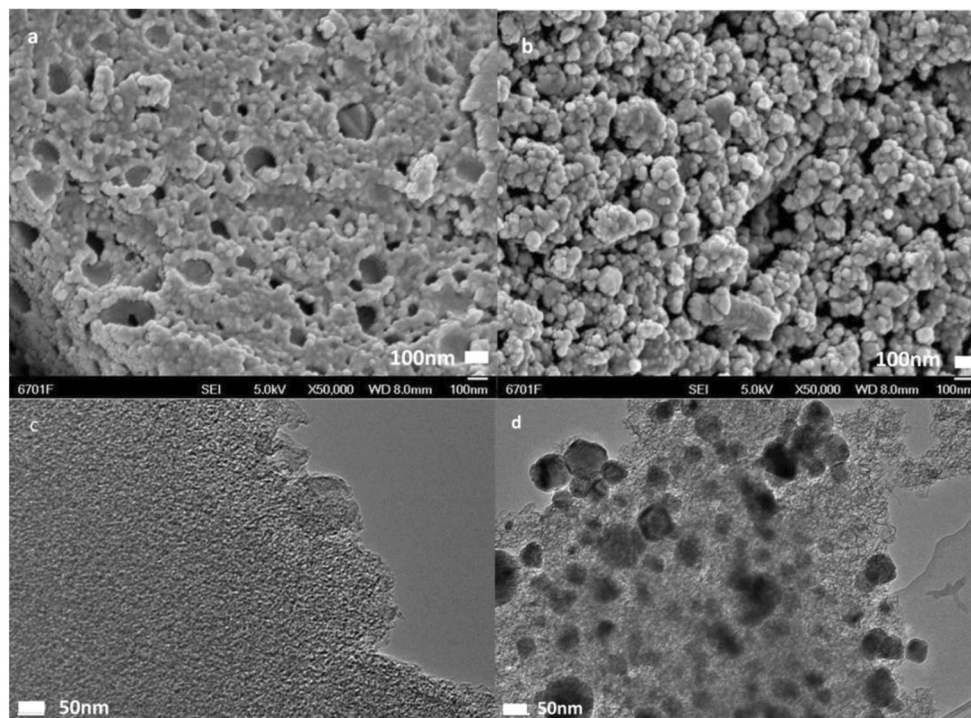


**Fig. 2** Infrared spectrum of the HAC

**Fig. 3** SEM images of (a) HAC and (b) Fe<sub>2</sub>O<sub>3</sub>/HAC. TEM images of (c) HAC and (d) Fe<sub>2</sub>O<sub>3</sub>/HAC



in Fig. 7b. HAC and Fe<sub>2</sub>O<sub>3</sub>/HAC have two characteristic peaks around 1335 cm<sup>-1</sup> and 1593 cm<sup>-1</sup>, respectively, corresponding to the G and D peaks of the carbon material, respectively. It is well known that the D band is closely related to the disordered carbon structure, and the G band is related to the SP<sup>2</sup> hybridization in the graphite structure [42, 43]. The intensity ratio ( $I_D/I_G$ ) between D band and G band is used to determine the degree of graphitization [44]. The  $I_D/I_G$  values of HAC and Fe<sub>2</sub>O<sub>3</sub>/HAC are calculated 1.19 and 1.18, indicating that the material has a certain degree of graphitization. In the Fe<sub>2</sub>O<sub>3</sub>/HAC, except for the obvious G and D peaks, characteristic Raman peaks of  $\alpha$ -Fe<sub>2</sub>O<sub>3</sub> are shown at 221, 293, 411, 607, and 1300 cm<sup>-1</sup> [45, 46], where the peaks of 1300 cm<sup>-1</sup> coincide with those of 1335 cm<sup>-1</sup> of carbon, and the narrow bands located at 221 and 411 cm<sup>-1</sup> can be assigned to the A<sub>1g</sub> modes, while the bands located at 293 and 607 cm<sup>-1</sup> are due to the E<sub>1g</sub> modes of  $\alpha$ -Fe<sub>2</sub>O<sub>3</sub>. The Raman spectrum confirms the

existence of  $\alpha$ -Fe<sub>2</sub>O<sub>3</sub>. Similarly, the characteristic peaks of Fe<sub>2</sub>O<sub>3</sub> nanomaterial are exactly the same as the peak positions of Fe<sub>2</sub>O<sub>3</sub>/HAC. The results of Raman and XRD also proved that Fe<sub>2</sub>O<sub>3</sub> nanoparticles were firmly grown on the HAC through hydrothermal reaction.

In order to analyze the chemical bonding states of the C, O, and Fe elements of the Fe<sub>2</sub>O<sub>3</sub>/HAC composite, we performed XPS characterization on the Fe<sub>2</sub>O<sub>3</sub>/HAC. As shown in Fig. 8a, the XPS spectrum of Fe<sub>2</sub>O<sub>3</sub>/HAC shows three different peaks, which are attributed to the C, O, and Fe elements, respectively. The C 1s spectrum mainly shows three peaks, as shown in Fig. 8b, located at 284.3, 285.1, and 286.4 eV, corresponding to the C-C sp<sup>2</sup>, C-C sp<sup>3</sup>, and C-O bonds, respectively [47]. For the O 1s spectrum, as shown in Fig. 8c, the peaks at 530.2, 531.1, and 533.7 eV correspond to the oxygen bonds of Fe-O, Fe-O-H, and H-O-H, respectively [48]. For the Fe 2p spectrum, it should be pointed out that Fe has more

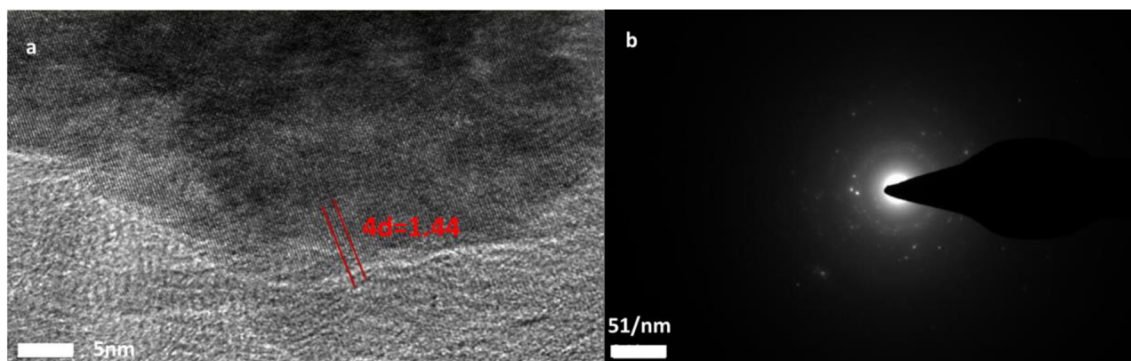


**Fig. 4** HRTEM image (a) and SAED pattern (b) of the Fe<sub>2</sub>O<sub>3</sub>/HAC

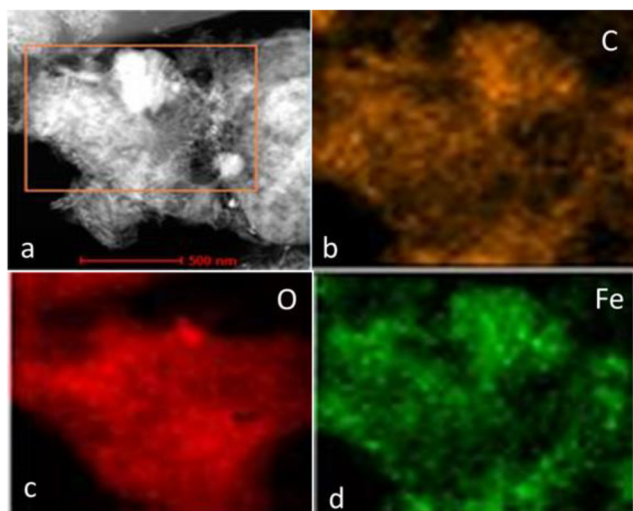
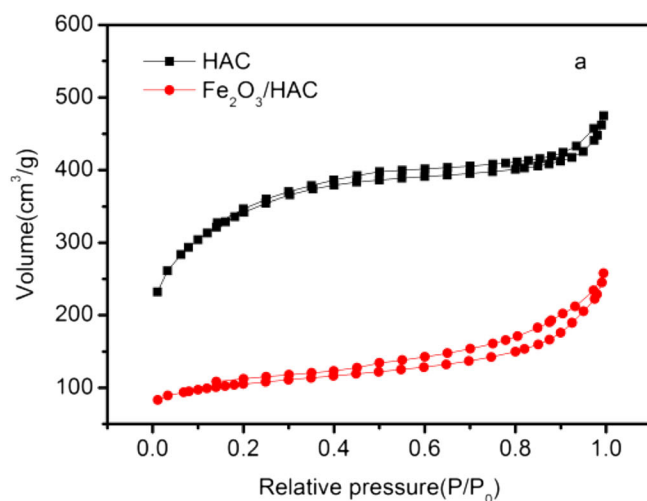


**Fig. 5** (a–d) EDX mapping of (b) C, (c) O, and (d) Fe elements in the  $\text{Fe}_2\text{O}_3/\text{HAC}$

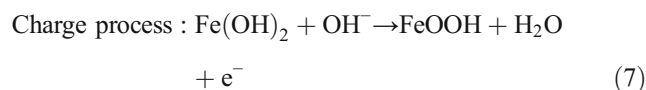
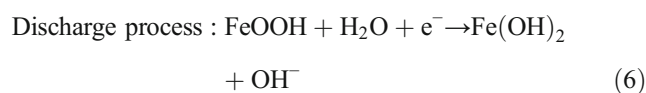
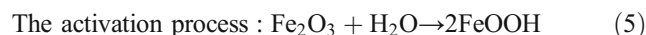
valence states and fewer differences in Fe 2p peaks. The photoelectric effect of Fe 3s electron can show different final states, it exhibits a unique bimodal structure behavior, and the spacing of this bimodal structure of Fe will change with the degree of Fe oxidation state, so it can be used to judge the oxidation state of Fe. From the Fe 2p spectrum shown in Fig. 8d, the electron binding energies of the two emission peaks are located at 711.7 and 725.3 eV corresponding to the spin orbits Fe  $2p_{3/2}$  and Fe  $2p_{1/2}$ , respectively. The binding energy interval is 13.6 eV, which is in consistent with the  $\alpha\text{-Fe}_2\text{O}_3$  reported in the literature [49, 50].

### 3.3. Characterization of electrochemical properties of materials

In three-electrode system, we used the HAC,  $\text{Fe}_2\text{O}_3$ , and  $\text{Fe}_2\text{O}_3/\text{HAC}$  as electrode materials to prepare working



electrodes and characterized their electrochemical performance. Figure 9a shows the cyclic voltammetry (CV) curves of the HAC,  $\text{Fe}_2\text{O}_3$ , and  $\text{Fe}_2\text{O}_3/\text{HAC}$ , which were tested between  $-1.2$  and  $-0.4$  V at  $10 \text{ mV s}^{-1}$ . We can see that the HAC shows a symmetrical rectangular shape, revealing its double electric layer capacitance performance, so the HAC can be used as a stable charge current collector to provide an effective ion transmission channel. Both the  $\text{Fe}_2\text{O}_3$  and  $\text{Fe}_2\text{O}_3/\text{HAC}$  clearly show a pair of redox peaks, with oxidation peaks at  $-0.652$  and  $-0.641$  V and reduction peaks at  $-0.996$  and  $-1.038$  V, respectively. Corresponding to the electrochemical reaction between  $\text{Fe}^{2+}$  and  $\text{Fe}^{3+}$  on the surface of the active material, the probable transformation reaction and charge storage mechanism is proposed as follows [51, 52]:



The integrated area of the  $\text{Fe}_2\text{O}_3/\text{HAC}$  curve is much larger than the integrated area of the  $\text{Fe}_2\text{O}_3$ , which is sufficient to show that the electrochemical behavior of the  $\text{Fe}_2\text{O}_3/\text{HAC}$  is the result of the synergistic effect of the two components HAC and  $\text{Fe}_2\text{O}_3$ . The HAC with porous structure provides more reactive sites for electrochemical reactions, enables more effective contact between the  $\text{Fe}_2\text{O}_3$  and the electrolyte, and provides more flow channels for the electrolyte, and it is beneficial to the electrolyte diffusion from the outside to the inside of the electrode material. Therefore, electrode materials made of composite materials include two processes: charging-discharging double-layer of porous carbon and charge transfer

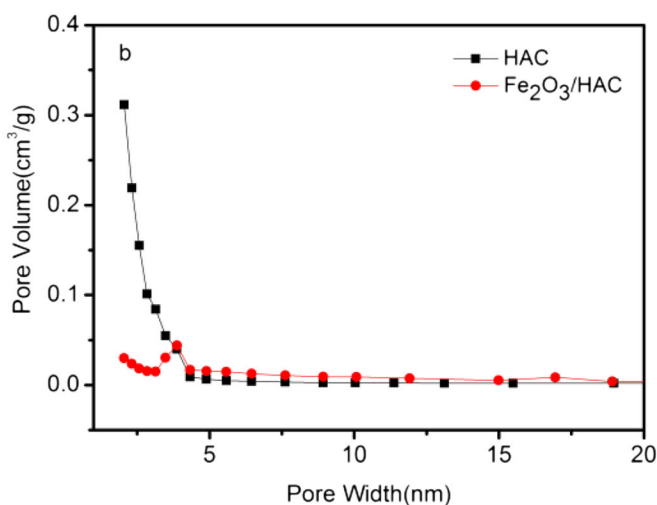


**Fig. 6** a  $\text{N}_2$  adsorption-desorption isotherms. b Pore size distributions of the HAC and  $\text{Fe}_2\text{O}_3/\text{HAC}$

**Table 1** Surface area and pore volume of the HAC and Fe<sub>2</sub>O<sub>3</sub>/HAC

Samples	S <sub>BET</sub> /m <sup>2</sup> g <sup>-1</sup>	V <sub>t</sub> /m <sup>3</sup> g <sup>-1</sup>	D <sub>av</sub> /nm	V <sub>me</sub> /m <sup>3</sup> g <sup>-1</sup>	V <sub>mi</sub> /m <sup>3</sup> g <sup>-1</sup>
HAC	1205.96	0.68	2.26	0.42	0.17
Fe <sub>2</sub> O <sub>3</sub> /HAC	366.82	0.34	3.79	0.30	0.09

process upon pseudocapacitance of Fe<sub>2</sub>O<sub>3</sub>-based. It is clear show that porous carbon materials have played a positive role in the electrochemical performance of pseudocapacitance. Figure 9b shows the CV curves of the Fe<sub>2</sub>O<sub>3</sub>/HAC at different scan rates from 5 to 50 mV s<sup>-1</sup> between -1.2 and -0.4 V. It can be seen from that the shape of the CV curves of the Fe<sub>2</sub>O<sub>3</sub>/HAC is maintained, with obvious pseudocapacitors properties, and the integral area increases with the increase of the scanning rate.

Figure 9c shows the galvanostatic charge-discharge (GCD) curves for the HAC, Fe<sub>2</sub>O<sub>3</sub>, and Fe<sub>2</sub>O<sub>3</sub>/HAC at the same current density of 1 A g<sup>-1</sup>. The Fe<sub>2</sub>O<sub>3</sub>/HAC shows longer discharge time. According to Eq. (1), the specific capacitances of the HAC, Fe<sub>2</sub>O<sub>3</sub>, and Fe<sub>2</sub>O<sub>3</sub>/HAC are 145, 90, and 256 F g<sup>-1</sup>, respectively. Obviously, the composite of HAC and Fe<sub>2</sub>O<sub>3</sub> increased the capacitance of Fe<sub>2</sub>O<sub>3</sub> by 2.8 times, showing a significant synergistic effect of 1 + 1 > 2. It is consistent with CV conclusion, which is sufficient to show that the electrochemical behavior of the Fe<sub>2</sub>O<sub>3</sub>/HAC is the result of the synergistic effect of the HAC and Fe<sub>2</sub>O<sub>3</sub>. Figure 9d shows the GCD curves of the Fe<sub>2</sub>O<sub>3</sub>/HAC at different current densities. We can see that the shape of the charge-discharge curve is maintained even at a high current density of 20 A g<sup>-1</sup>. In Fig. 9e, it shows the variation rate performances of the three samples. The specific capacitance of Fe<sub>2</sub>O<sub>3</sub>/HAC is much higher than that of the two separate electrode materials, which further shows that the composite materials have better electrochemical performance than the two separate materials.

In order to deep insight the effect of porous carbon-based materials on the electrochemical performance of composite materials, EIS measurements were performed; the results are shown in Fig. 9f. The corresponding equivalent circuit for impedance analysis is shown in the inset of Fig. 9f, which consists of a series and parallel combination of resistances, R<sub>s</sub> (contribution of ionic resistance of electrolyte, intrinsic resistance of substrate, and contact resistance between active material and current collector), R<sub>ct</sub> (charge transfer resistance), CPE (constant phase element), and W (Warburg impedance) [53]. In the high-frequency region, from the embedded figure of 4.9 (f), we can calculate that the internal resistances of HAC, Fe<sub>2</sub>O<sub>3</sub>, and Fe<sub>2</sub>O<sub>3</sub>/HAC are 1.04, 0.94, and 0.80 Ω, respectively. It can be seen that the Fe<sub>2</sub>O<sub>3</sub>/HAC has the smallest internal resistance due to the porosity and good dispersibility. The oblique line in the low-frequency region is related to the ion diffusion and capacitance characteristics. The closer the straight line in the low-frequency region is to the vertical axis, the better the capacitance performance of the electrode material is. From the BET analysis, it can be concluded that the HAC has the largest pore distribution, so its ion diffusion performance is the best, and its straight line slope in the low-frequency region is the largest. However, the Fe<sub>2</sub>O<sub>3</sub>/HAC also has good ion diffusivity. In general, the electrochemical impedance performance of the Fe<sub>2</sub>O<sub>3</sub>/HAC has almost the same characteristics of an ideal capacitor material.

In addition, the linear relationship between the anode and cathode peak currents (i<sub>p</sub>) and scan rate (v) is a meaningful

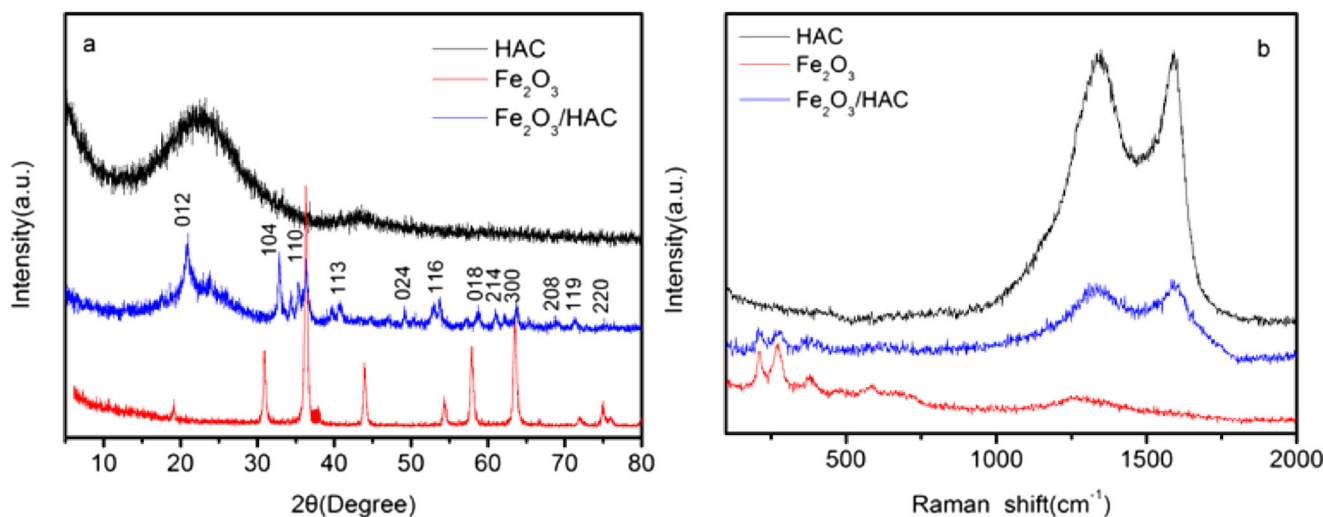


**Fig. 7** a XRD patterns. b Raman spectra of the HAC, Fe<sub>2</sub>O<sub>3</sub>, and Fe<sub>2</sub>O<sub>3</sub>/HAC

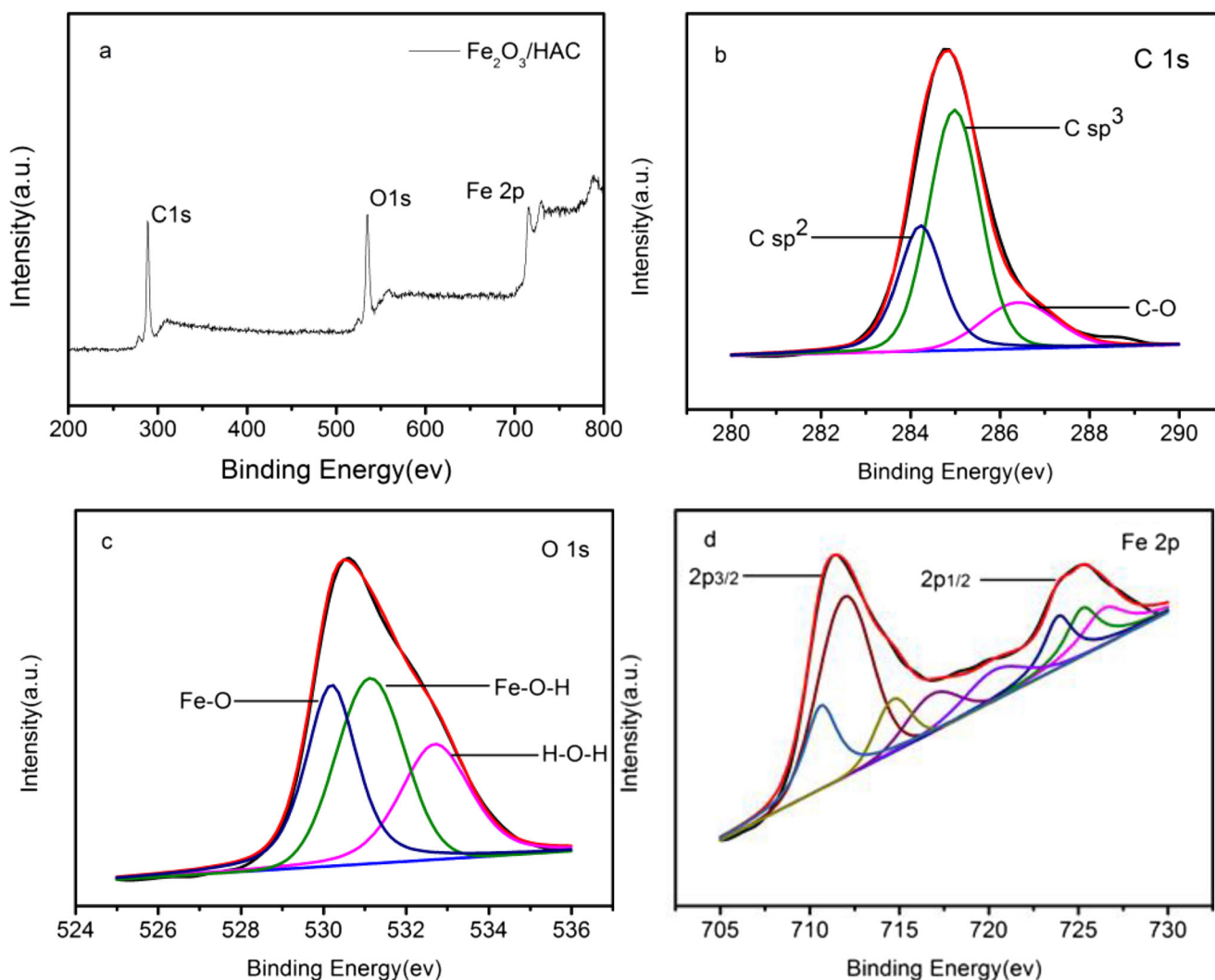


**Fig. 8** XPS spectrum of the  $\text{Fe}_2\text{O}_3/\text{HAC}$ : (a) survey spectrum, (b) C 1s, (c) O 1s, and (d) Fe 2p

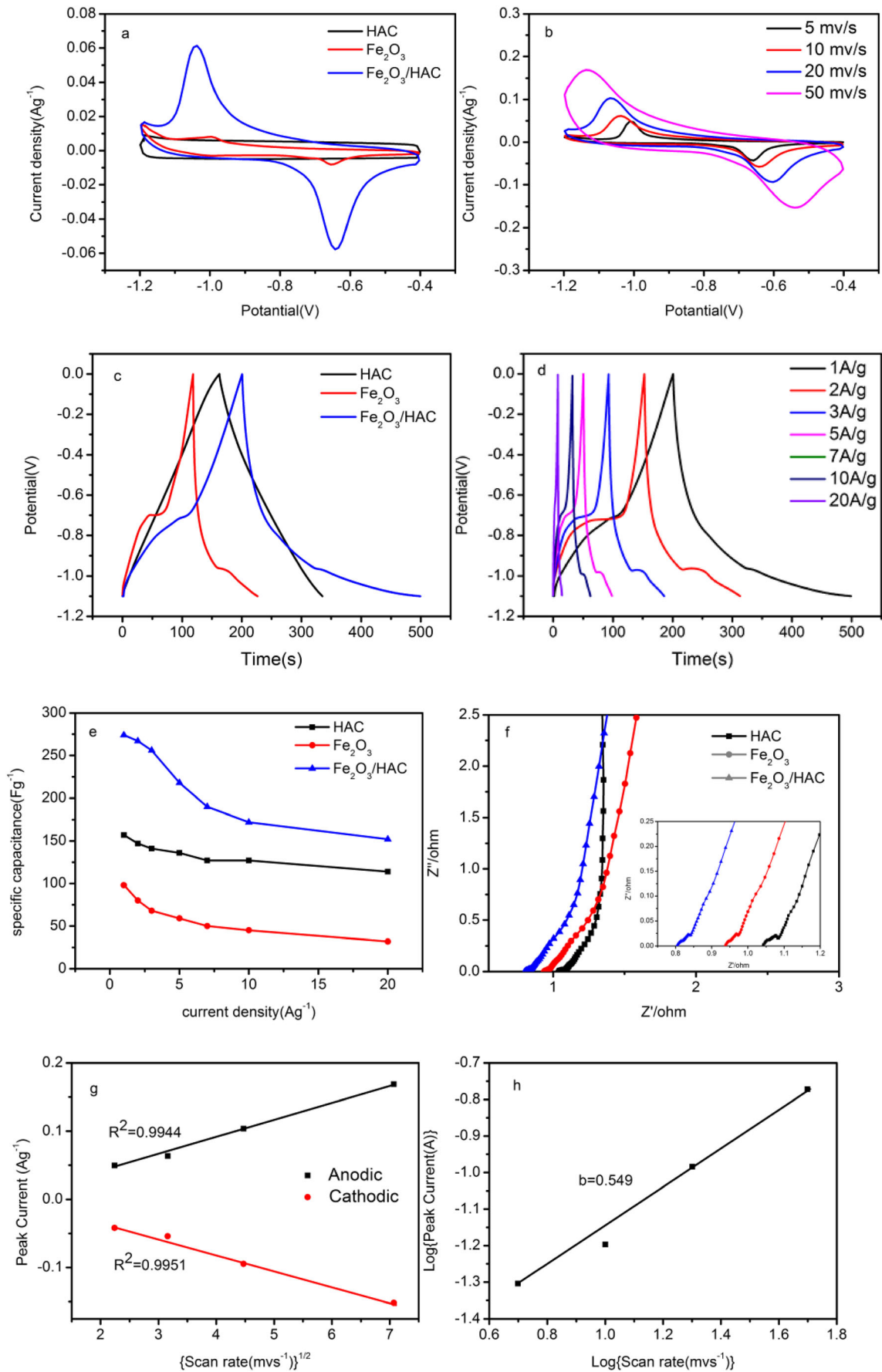
parameter that can better understand the dynamic effects of electrode materials, as shown in Fig. 9g. Mathematically, the peak current can be expressed as  $i_p = a v^b$ , where  $a$  and  $b$  are constants and  $v$  is the scan rate. The calculated  $b$  value is used to identify the type of kinetic mechanism involved in the capacitor unit [54]. By fitting  $\text{Fe}_2\text{O}_3/\text{HAC}$  to the scanning rate range of  $5\text{--}50 \text{ mV s}^{-1}$ , the correlation coefficient ( $R^2$ ) of  $b$  is 0.9944 for anode peak and 0.9951 for cathode peak. The results show that the peak current has a good linear relationship with the scanning rate. The  $\log(\text{anode current})\text{--}\log(\text{scan rate})$  curve was plotted according to  $i_p = a v^b$  (Fig. 9h). It can be seen that the coefficient  $b = 0.543$  is calculated, which means the redox process of the redox medium is limited by the surface reaction of the electrode with  $\text{Fe}_2\text{O}_3$  and also demonstrated the fast kinetics of the  $\text{Fe}_2\text{O}_3$  [55].

Figure 9i shows the contrast of long-cycle stability of the  $\text{Fe}_2\text{O}_3$  and  $\text{Fe}_2\text{O}_3/\text{HAC}$ . With the increase of charge and discharge time, the capacitance decreased continuously. For the electrode with  $\text{Fe}_2\text{O}_3$ , the capacitance retention rate was

52.2% after 1000 cycles, while for the electrode with  $\text{Fe}_2\text{O}_3/\text{HAC}$ , the capacitance retention rate was 72.6% after 1000 cycles. The excellent cycling stability of the  $\text{Fe}_2\text{O}_3/\text{HAC}$  electrode can be attributed to the favorable function of hemp straw-based porous carbon for anchoring nanosized  $\text{Fe}_2\text{O}_3$  particles, which effectively prevent the aggregation of these

**Fig. 9** Electrochemical evaluation of the HAC,  $\text{Fe}_2\text{O}_3$  and  $\text{Fe}_2\text{O}_3/\text{HAC}$  in three-electrode system. **a** CV curves for the HAC,  $\text{Fe}_2\text{O}_3$ , and  $\text{Fe}_2\text{O}_3/\text{HAC}$  at a scan rate of  $10 \text{ mV s}^{-1}$ . **b** CV curves for the  $\text{Fe}_2\text{O}_3/\text{HAC}$  at scan rates ranging from 5 to  $50 \text{ mV s}^{-1}$ . **c** GCD curves of the HAC,  $\text{Fe}_2\text{O}_3$ , and  $\text{Fe}_2\text{O}_3/\text{HAC}$  at the current density of  $1 \text{ A g}^{-1}$ . **d** GCD curves of the  $\text{Fe}_2\text{O}_3/\text{HAC}$  at different current densities. **e** Specific capacitance of the HAC,  $\text{Fe}_2\text{O}_3$ , and  $\text{Fe}_2\text{O}_3/\text{HAC}$  at densities from 1 to  $20 \text{ A g}^{-1}$ . **f** EIS of the HAC,  $\text{Fe}_2\text{O}_3$ , and  $\text{Fe}_2\text{O}_3/\text{HAC}$ . **g** Linear relationship of anodic and cathodic peak current with square root of scan rate for the  $\text{Fe}_2\text{O}_3/\text{HAC}$ . **h** The  $b$  value determination of peak current of anode over a wide scan rate range from 5 to  $50 \text{ mV s}^{-1}$  for the  $\text{Fe}_2\text{O}_3/\text{HAC}$ . **i** Cyclic stability performance of the  $\text{Fe}_2\text{O}_3$  and  $\text{Fe}_2\text{O}_3/\text{HAC}$  at the current density of  $2 \text{ A g}^{-1}$  after 1000 cycles





nanoparticles. Furthermore, because of the poor mechanical properties of iron oxides,  $\text{Fe}_2\text{O}_3$  particles may suffer structural collapse during the long-time charge-discharge process, resulting in a rapid decrease in capacitance. Therefore, the cycle stability and cycle life of the  $\text{Fe}_2\text{O}_3/\text{HAC}$  electrode could be improved by the addition of hemp straw-based porous carbon. In a word, the effective recombination of materials provides more structural advantages, which is necessary for the long-term charge storage.

To further explore the possibility of the  $\text{Fe}_2\text{O}_3/\text{HAC}$  in practical application, the symmetrical supercapacitor device was assembled with two identical  $\text{Fe}_2\text{O}_3/\text{HAC}$  electrodes ( $\text{Fe}_2\text{O}_3/\text{HAC}/\text{Fe}_2\text{O}_3/\text{HAC}$ ). Figure 10a shows the CV curves of the device at scan rates from 5 to 100  $\text{mV s}^{-1}$ . It can be observed that the rectangle of the curves remain the same at all scan rates, which indicates the ideal capacitor performance. Figure 10b shows that during the measurement of current density from 1 to 20  $\text{A g}^{-1}$ , the GCD curves of the device

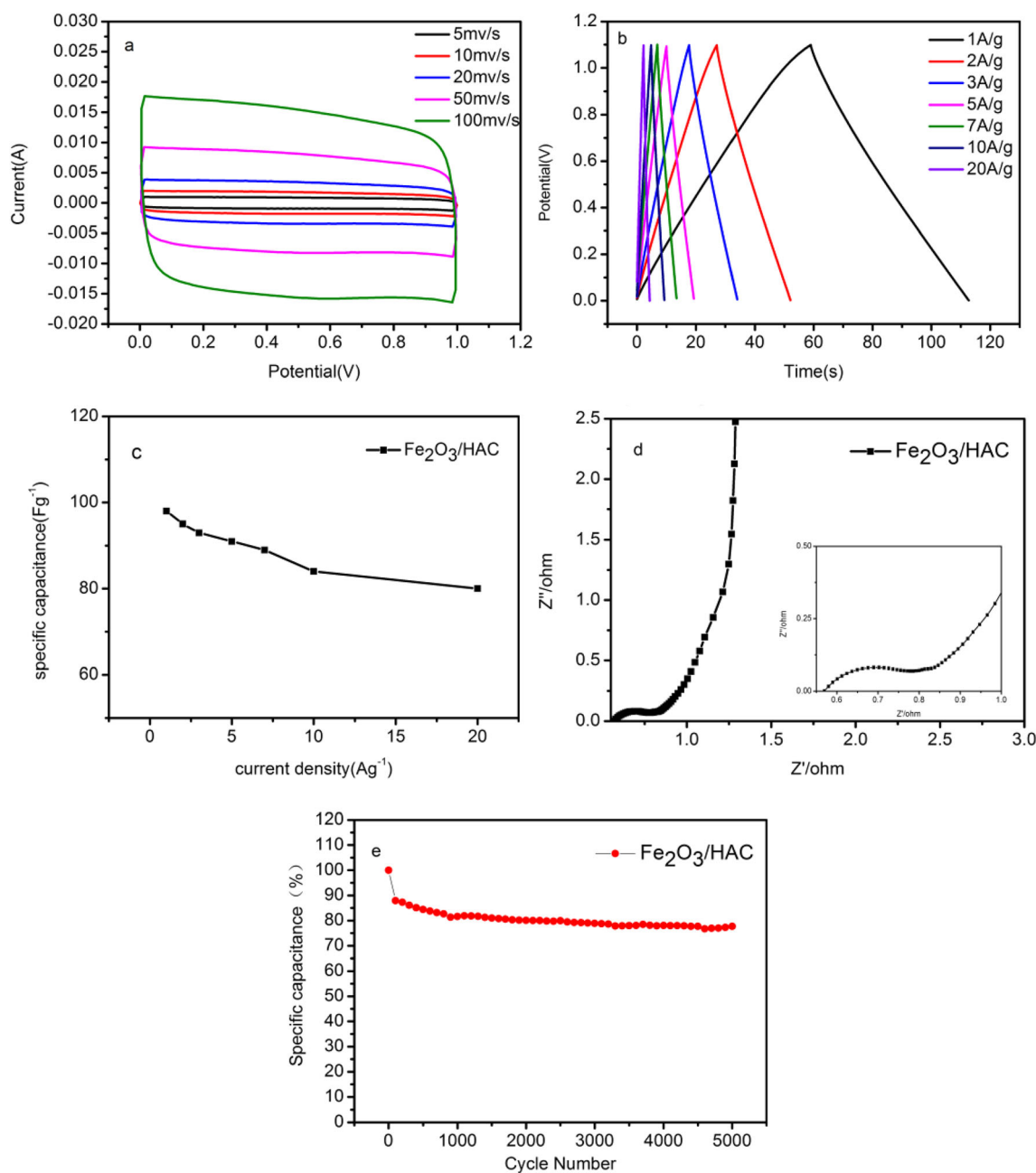


**Fig. 10** Electrochemical performance of the symmetrical supercapacitor device. **a** CV curves at scan rates ranging from 5 to 100  $\text{mV s}^{-1}$ . **b** GCD curves at different current densities. **c** Specific capacitance of the device at

densities from 1 to 20  $\text{A g}^{-1}$ . **d** EIS of the device. **e** Cycling stability performance at the current density of 2  $\text{A g}^{-1}$  after 5000 cycles

show good symmetry, high coulomb efficiency, and electrochemical reversibility. According to Eq. (2), the device has specific capacitance of  $98.7 \text{ F g}^{-1}$  of  $1 \text{ A g}^{-1}$ . It can still be maintained at  $83.6 \text{ F g}^{-1}$  and  $20 \text{ A g}^{-1}$ . The specific capacitance of different electrodes calculated from the discharge curves at different current densities is given in Fig. 10c. It can be seen that when changing from  $1$  to  $20 \text{ A g}^{-1}$ , the specific capacitance retention rate is  $82.1\%$ , which means that excellent stability is maintained throughout the charge and discharge process.

The EIS curve of the symmetrical supercapacitor device is shown in Fig. 10d. It can be seen that the cross point of the real axis reflects the small internal resistance of the electrode material, which is  $0.49 \Omega$ . The semicircle corresponds to the charge transfer resistance. The small radius of the curve in the high-frequency region means that it has a smaller charge transfer resistance. In the low-frequency region, the straight line which tends to be almost vertical represents the diffusion resistance and mass transfer rate of electrolyte in the electrode hole. Therefore, the device has excellent capacitance characteristics in impedance performance.

Figure 10e shows the cyclic stability of the supercapacitor device at constant current density of  $2 \text{ A g}^{-1}$ . After the initial cycling, the specific capacitance of the capacitor remains basically stable. During 5000 consecutive cycles, the capacitance value remained at  $77.71\%$  of its initial capacitance value, which indicates that the device has excellent cycle stability performance. The initial quick drop in the specific capacitance is presumably a result of structural changes in the electrode material. After the first charge-discharge process, the invalid pore structure in the composite was collapsed. After entering the second cycle, the specific capacitance of the capacitor remains basically stable.

## 4. Conclusion

In this study, we used the porous carbon prepared from biomass hemp straw as the carbon-based material to load  $\text{Fe}_2\text{O}_3$  evenly. In this way, the carbon-based material provides stable loading site for metal oxides, while its porous structure channels are conducive to the ion transport in the electrolyte and provide part of the double-layer electric capacity. The  $\text{Fe}_2\text{O}_3$  is well dispersed and produce larger pseudocapacitors. Therefore, the specific capacitance and cycle stability of the electrode can be effectively improved by the cooperation between the double-layer capacitor and the pseudocapacitor, so that the electrode material can be greatly improved to obtain better electrochemical performance. This low-cost, simple, and effective method for the production of electrode materials is expected to be used for the preparation of other metal oxide composites.

**Funding information** This work was supported by the National Natural Science Foundation of China [21567015, 21407072]; the CAS “Light of West China” Program; the National Key R&D Program of China [2016YFC0202900]; the Natural Science Foundation of Gansu Province [17JR5RA109]; the Gansu Provincial Institutions of Higher Learning Innovation Ability Promotion Project(2019A-220); the Gansu Province College Student Innovation and Entrepreneurship Training Program Project; and the Lanzhou University of Technology Hongliu First-class Discipline Construction Program.

## References

- Simon P, Gogotsi Y (2013) Capacitive energy storage in nanostructured carbon-electrolyte systems. *Acc Chem Res* 46(5):1094–1103
- Ekrani E, Dadashian F, Soleimani M (2014) Waste cotton fibers based activated carbon: optimization of process and product characterization. *Fiber Polym* 15:1855–1864
- Duggal AR, Levinson LM (1997) A novel high current density switching effect in electrically conductive polymer composite materials. *J Appl Phys* 82(11):5532–5539
- Sun L, Tian C, Li M, Meng X, Wang L, Wang R, Yin J, Fu H (2013) From coconut shell to porous grapheme-like nanosheets for high-power supercapacitors. *J Mater Chem* 1(21):6462–6477
- Zhang G, Xiao X, Li B, Gu P, Xue H, Pang H (2017) Transition metal oxides with one-dimensional/one-dimensional-analogue nanostructures for advanced supercapacitors. *J Mater Chem* 5(18):1024–1039
- Chen F, Zhang X, Liang H, Kong M, Guan Q, Chen P, Wu Z, Yu S (2012) Synthesis of nitrogen-doped porous carbon nanofibers as an efficient electrode material for supercapacitors. *ACS Nano* 6(8):7092–7102
- Lochmann S, Grothe J, Kai E, Leistenschneider D, Borchardt L, Kaskel S (2018) Nanoimprint lithography of nanoporous carbon materials for micro-supercapacitor architectures. *Nanoscale* 10(21):10109–10115
- Li Z, Yang L, Cao H, Chang Y, Tang K, Cao Z, Chang J, Cao Y, Wang W, Gao M (2017) Carbon materials derived from chitosan/cellulose cryogel-supported zeolite imidazole frameworks for potential supercapacitor application. *Carbohydr Polym* 175(1):223–230
- Tooming T, Thomberg T, Romann T, Palm R, Lust E (2013) Carbon materials for supercapacitor application by hydrothermal carbonization of D-glucose. *Iop Conf* 49:2013–2022
- Frackowiak E (2007) Carbon materials for supercapacitor application. *Phys Chem Chem Phys* 9(15):1774–1785
- Li Y, Meng Q, Zhu SM, Sun ZH, Yang H, Chen ZX, Zhu CL, Guo ZP, Zhang D (2015) A Fe/Fe<sub>3</sub>O<sub>4</sub>/N-carbon composite with hierarchical porous structure and in situ formed N-doped graphene-like layers for high-performance lithium ion batteries. *Dalton Trans* 44(10):4594–4600
- Huang L, Chen D, Ding Y, Feng S, Liu M (2013) Nickel-cobalt hydroxide nanosheets coated on NiCo<sub>2</sub>O<sub>4</sub> nanowires grown on carbon fiber paper for high-performance pseudocapacitors. *Nano Lett* 13(7):3135–3139
- Luo B, Yang H, Liu S, Fu W, Sun P, Yuan M, Zhang Y, Liu Z (2008) Fabrication and characterization of self-organized mixed oxide nanotube arrays by electrochemical anodization of Ti-6Al-4V alloy. *Mater Lett* 62(30):4512–4515
- Ma M, Zhu Y, Sun Q, Li X, Su J, Zhao L, Zhao Y, Qiu S, Yan W, Wang K (2015) The asymmetric synthesis of CF<sub>3</sub>-containing spiro [pyrrolidin-3, 2-oxindole] through the organocatalytic 1,3-dipolar cycloaddition reaction. *Chem Commun* 51(42):8789–8792
- Sun Q, Li X, Su J, Zhao L, Ma M, Zhu Y, Zhao Y, Zhu R, Yan W, Wang K (2015) The squaramide-catalyzed 1,3-dipolar

- cycloaddition of nitroalkenes with N-2,2,2-trifluoroethylsatin ketimines: an approach for the synthesis of 5'-trifluoromethylspiro[pyrrolidin-3,2'-oxindoles]. *Adv Synth Catal* 357(14–15): 3187–3196
16. Liu S, Fu W, Yang H, Li M, Peng S, Luo B, Yu Q, Wei R, Yuan M, Zhang Y (2010) Synthesis and characterization of self-organized oxide nanotube arrays via a facile electrochemical anodization. *China Ceramics* 10(7):227–230
  17. Lu Q, Chen JG, Xiao JQ (2013) Nanostructured electrodes for high-performance pseudocapacitors. *Angew Chem Int Ed* 52(7):1882–1889
  18. Xu C, Li Z, Yang C, Zou P, Xie B, Lin Z, Zhang Z, Li B, Kang F, Wong C (2016) An ultralong, highly oriented nickel-nanowire-array electrode scaffold for high-performance compressible pseudocapacitors. *Adv Mater* 28(21):4105–4110
  19. Liu L, Zhao H, Lei Y (2019) Nanoarchitected current collectors: review on nanoarchitected current collectors for pseudocapacitors. *Small Methods* 3(8):231–244
  20. Deng T, Zhang W, Arcelus O, Kim JG, Rojo T (2017) Atomic-level energy storage mechanism of cobalt hydroxide electrode for pseudocapacitors. *Nat Commun* 8:15194–15203
  21. Nithya VD, Arul NS (2016) Review on  $\alpha$ - $\text{Fe}_2\text{O}_3$  based negative electrode for high performance supercapacitors. *J Power Sources* 327:297–318
  22. Nithya VD, Sabari AN (2016) Progress and development of  $\text{Fe}_3\text{O}_4$  electrodes for supercapacitors. *J Mater Chem A* 4(28):10767–10778
  23. Zeng Y, Yu M, Meng Y, Fang P, Lu X, Tong Y (2016) Iron-based supercapacitor electrodes: advances and challenges. *Adv Energy Mater* 6(24):1601053–1601070
  24. Lee LL, Deng S, Fan HM, Mhaisalkar S, Tan HR, Tok ES (2012)  $\alpha$ - $\text{Fe}_2\text{O}_3$  nanotubes-reduced graphene oxide composites as synergistic electrochemical capacitor materials. *Nanoscale* 4(9):2958–2961
  25. Low QX, Ho GW (2014) Facile structural tuning and compositing of iron oxide-graphene anode towards enhanced supercapacitive performance. *Nano Energy* 5:28–35
  26. Sethuraman B, Purushothaman KK, Muralidharan G (2013) Synthesis of mesh-like  $\text{Fe}_2\text{O}_3/\text{C}$  nanocomposite via greener route for high performance supercapacitors. *RSC Adv* 4(9):4631–4612
  27. Prade T, Svensson S, Andersson A, Mattsson JE (2011) Biomass and energy yield of industrial hemp grown for biogas and solid fuel. *Biomass Bioenergy* 35(7):3040–3049
  28. Paredes JI, Villar-Rodil S, Marti Nez-Alonso A, Tasco NJMD (2008) Graphene oxide dispersions in organic solvents. *LANGMUIR* 24(19):10560–10564
  29. Guan D, Gao Z, Yang WL, Wang J, Yuan Y, Wang B, Zhang ML, Liu LH (2013) Hydrothermal synthesis of carbon nanotube/cubic  $\text{Fe}_3\text{O}_4$  nanocomposite for enhanced performance supercapacitor electrode material. *Mater Sci Eng B* 178(10):736–743
  30. Tan Z, Chen G, Zhu Y (2011) Carbon-based Supercapacitors produced by the activation of graphene. *John Wiley & Sons Ltd* 332(6037):1537–1542
  31. Hu Y, Guan C, Ke Q, Yow ZF, Cheng C, Wang J (2016) Hybrid  $\text{Fe}_2\text{O}_3$  nanoparticle clusters/rGO paper as an effective negative electrode for flexible Supercapacitors. *Chem Mater* 28(20):2576–2585
  32. Owusu KA, Qu L, Li J, Wang Z, Zhao K, Yang C, Hercule KM, Lin C, Shi C, Wei Q (2017) Low-crystalline iron oxide hydroxide nanoparticle anode for high-performance supercapacitors. *Nat Commun* 8:14264–14273
  33. Thommes M (2016) Physisorption of gases, with special reference to the evaluation of surface area and pore size distribution (IUPAC technical report). *Pure Appl Chem* 38(1):25–32
  34. Lu W, Sevilla M, Fuertes AB, Mokaya R, Yushin G (2011) Hydrothermal carbonization of abundant renewable natural organic chemicals for high-performance supercapacitor electrodes. *Adv Energy Mater* 1(3):356–361
  35. Wakeland S, Martinez R, Grey JK, Luhrs CC (2010) Production of graphene from graphite oxide using urea as expansion-reduction agent. *Carbon* 48(12):3463–3470
  36. Klahr BM, Martinson ABF, Hamann TW (2011) Photoelectrochemical investigation of ultrathin film iron oxide solar cells prepared by atomic layer deposition. *LANGMUIR* 27(1): 461–468
  37. Guan LJ, Wang Y, Mao L, Fan Z, Shen Z, Zhang H, Wang J (2015) Iron oxide-decorated carbon for supercapacitor anodes with ultrahigh energy density and outstanding cycling stability. *ACS Nano* 9(5):5198–5207
  38. Binitha G, Soumya MS, Madhavan AA, Praveen P, Sivakumar N (2013) Electrospun  $\alpha$ - $\text{Fe}_2\text{O}_3$  nanostructures for supercapacitor applications. *J Mater Chem A* 1(38):11698–11704
  39. Fan ZI, Qin XU, Sun HU, Zhu ZI, Deng WI (2013) Superhydrophobic mesoporous graphene for separation and absorption. *Chem Plus Chem* 78(10):1282–1287
  40. Jawhari T, Roid A, Casado J (1995) Raman spectroscopic characterization of some commercially available carbon black materials. *Carbon* 33(11):1561–1565
  41. Luo C, Niu S, Zhou G, Lv W, Li B, Kang F, Yang QH (2016) Dual-functional hard template directed one-step formation of a hierarchical porous carbon-carbon nanotube hybrid for lithium-sulfur batteries. *Chem Commun* 52(82):12143–12146
  42. Fei H, Peng Z, Li L, Yang Y, Wei L, Errol LGS, Xiu F, James MT (2014) Preparation of carbon-coated iron oxide nanoparticles dispersed on graphene sheets and applications as advanced anode materials for lithium-ion batteries. *Nano Res* 7(4):1–9
  43. Reddy MV, Yu T, Sow CH, Shen ZX, Lim CT, Subba Rao GV, Chowdari BVR (2007)  $\alpha$ - $\text{Fe}_2\text{O}_3$  Nanoflakes as an anode material for Li-ion batteries. *Adv Funct Mater* 17(15):2792–2799
  44. Jeong JM, Choi BG, Lee SC, Lee KG, Huh YS (2013) Hierarchical hollow spheres of  $\text{Fe}_2\text{O}_3$ @polyaniline for lithium ion battery anodes. *Adv Mater* 25(43):6250–6255
  45. Zhou Y, Ma R, Candelaria SL, Wang J, Liu Q, Uchaker E, Li P, Chen Y, Cao G (2016) Phosphorus/sulfur co-doped porous carbon with enhanced specific capacitance for supercapacitor and improved catalytic activity for oxygen reduction reaction. *J Power Sources* 314:39–48
  46. Long C, Jiang L, Wei T, Yan J, Fan Z (2014) High-performance asymmetric supercapacitors with lithium intercalation reaction using metal oxide-based composites as electrode materials. *J Mater Chem A* 2(39):16678–16686
  47. Suresh R, Giribabu K, Manigandan R, Stephen A, Narayanan V (2014) Fabrication of Ni- $\text{Fe}_2\text{O}_3$  magnetic nanorods and application to the detection of uric acid. *RSC Adv* 4(33):17146–17155
  48. Yang P, Yong D, Lin Z, Chen Z, Zhong LW (2014) Low-cost high-performance solid-state asymmetric supercapacitors based on  $\text{MnO}_2$  nanowires and  $\text{Fe}_2\text{O}_3$  nanotubes. *Nano Lett* 14(2):731–736
  49. Liu J, Chen M, Zhang L, Jiang J, Yan J, Huang Y, Lin J, Fan HJ, Shen ZX (2014) A flexible alkaline rechargeable Ni/Fe battery based on Graphene foam/carbon nanotubes hybrid film. *Nano Lett* 14(12):7180–7187
  50. Wang H, Xu Z, Yi H, Wei H, Guo Z, Wang X (2014) One-step preparation of single-crystalline  $\text{Fe}_2\text{O}_3$  particles/graphene composite hydrogels as high performance anode materials for supercapacitors. *Nano Energy* 7:86–96
  51. Yoo H, Min M, Bak S, Yoon Y, Lee H (2014) A low ion-transfer resistance and high volumetric supercapacitor using hydrophilic surface modified carbon electrodes. *J Mater Chem A* 2(18):6663–6668
  52. Sodtipinta J, Amornsakchai T, Pakawatpanurut P (2017) Nanoporous carbon derived from agro-waste pineapple leaves for

- supercapacitor electrode. *Adv Nat Sci Nanosci Nanotechnol* 8(3): 35017–35028
53. Chao D, Liang P, Chen Z, Bai L, Shen ZX (2016) Pseudocapacitive Na-ion storage boosts high-rate and areal capacity of self-branched 2D layered metal chalcogenide nanoarrays. *ACS Nano* 10(11): 10211–10219
54. Zhan D, Ni Z, Chen W, Sun L, Luo Z, Lai L, Yu T, Wee ATS, Shen Z (2011) Electronic structure of graphite oxide and thermally reduced graphite oxide. *Carbon* 49(4):1362–1366
55. Zhang D, Hao Y, Zheng L, Ma Y, Feng H, Luo H (2013) Nitrogen and sulfur co-doped ordered mesoporous carbon with enhanced electrochemical capacitance performance. *J Mater Chem A* 1(26): 7584–7596

**Publisher's note** Springer Nature remains neutral with regard to jurisdictional claims in published maps and institutional affiliations.